PHYSICS

Electrical 180° switching of Néel vector in spin-splitting antiferromagnet

Lei Han[1]†, Xizhi Fu[2]†, Rui Peng[2], Xingkai Cheng[2], Jiankun Dai[1], Liangyang Liu[3], Yidian Li[3], Yichi Zhang[1], Wenxuan Zhu[1], Hua Bai[1], Yongjian Zhou[1], Shixuan Liang[1], Chong Chen[1], Qian Wang[1], Xianzhe Chen[1], Luyi Yang[3,4,5], Yang Zhang[6,7], Cheng Song[1]*, Junwei Liu[2]*, Feng Pan[1]*

Antiferromagnetic spintronics have attracted wide attention due to its great potential in constructing ultradense and ultrafast antiferromagnetic memory that suits modern high-performance information technology. The electrical 180° switching of Néel vector is a long-term goal for developing electrical-controllable antiferromagnetic memory with opposite Néel vectors as binary "0" and "1." However, the state-of-art antiferromagnetic switching mechanisms have long been limited for 90° or 120° switching of Néel vector, which unavoidably require multiple writing channels that contradict ultradense integration. Here, we propose a deterministic switching mechanism based on spin-orbit torque with asymmetric energy barrier and experimentally achieve electrical 180° switching of spin-splitting antiferromagnet Mn_5Si_3. Such a 180° switching is read out by the Néel vector–induced anomalous Hall effect. On the basis of our writing and readout methods, we fabricate an antiferromagnet device with electrical-controllable high- and low-resistance states that accomplishes robust write and read cycles. Besides fundamental advance, our work promotes practical spin-splitting antiferromagnetic devices based on spin-splitting antiferromagnet.

INTRODUCTION

One of the most well-known applications of spintronics is the electrical-controllable nonvolatile magnetic random-access memory (MRAM), where the information states "1" and "0" are stored by the up and down directions of the order parameter in ferromagnet (FM), i.e., the magnetic moment (*1–3*). For the original MRAM, the electrical read is based on tunneling magnetoresistance (*4–6*) (TMR), and the electrical write is realized by applying current along single channel to switch the magnetic moment due to spin transfer torques (*7, 8*). Over the past decades, although many emerging effects such as spin-orbit torques (SOTs) switching (*9, 10*) have improved the performance of MRAM, intrinsic large stray fields and gigahertz dynamics of FM fundamentally limit MRAM from achieving future breakthroughs in high-density integration and high-speed operation (*11, 12*). Besides, a very small magnetic field may be able to switch the direction of magnetic moment in MRAM, challenging its data storage stability (*11, 12*). Supreme to FM counterparts, antiferromagnet (AFM) exhibits tremendous potential for building ultradense and ultrafast AFM-RAM with high immunity to magnetic field disturbance thanks to their intrinsic advantages of zero stray field, terahertz dynamics, and compensated moment (*13–17*). With TMR predicted (*18, 19*) and found (*20, 21*) recently in many AFMs, the long-desired electrical-controllable AFM-RAM becomes possible as long as the

electrical switching of the AFM order parameter (i.e., the Néel vector) can be achieved.

However, the state-of-art reorientation of Néel vectors are all in-plane 90° or 120° switching by SOTs, which inevitably require multiple writing channels, leading to huge integration difficulties for AFM-RAM (*13, 22–24*). Similar to FM MRAM, practical AFM-RAM undoubtably needs electrical current along single writing channel to switch the Néel vector back and forth, which generates high and low resistance to represent binary "1" and "0" (*11*). An ideal solution is the 180° switching of Néel vectors back and forth ($n_+ \leftrightarrow n_-$) in AFMs by electrical current with opposite polarities along single writing channel. Moreover, 180° switching is truly needed to generate substantial antiferromagnetic TMR (*18, 19*). Therefore, electrical 180° switching of Néel vector is very important but remains unveiled.

The core difficulty of electrical 180° switching of Néel vector lies in equal energy barriers for $n_+ \rightarrow n_-$ and $n_- \rightarrow n_+$, defined by uniaxial magnetic anisotropy. In this case, if SOTs drive the Néel vector to rotate from n_+ to n_- by overcoming the energy barrier for $n_+ \rightarrow n_-$, it can also continuously drive the Néel vector to rotate from n_- to n_+ (*23*), which makes the 180° switching of Néel vector nondeterministic. That is why the more promising 180° switching of Néel vector remains unrealized for a long time since the first discovery of 90° switching of Néel vector in 2016 (*13*). Note that the 180° switching of CuMnAs by staggered spin-orbit fields is actually due to antiferromagnetic domain wall motion instead of the most desired deterministic 180° switching of Néel vector (*25*). Besides, the 180° switching of perpendicular cluster magnetic octuple has been achieved in noncollinear AFM (ncAFM) Mn_3Sn, but it is fundamentally different from 180° switching of Néel vector as the order parameter in collinear AFM (cAFM) (*26, 27*). Another important difficulty is to read out the 180° switching of Néel vector. Antiferromagnetic anisotropic magnetoresistance has been widely adopted, but it cannot read out 180° switching (*13, 22–24*). Harmonic measurements need specific sublattice symmetry breaking, which is not general and is hard to implement (*25*). Fortunately, the 180° switching of Néel vector may be feasibly

[1]Key Laboratory of Advanced Materials (MOE), School of Materials Science and Engineering, Tsinghua University, Beijing 100084, China. [2]Department of Physics, Hong Kong University of Science and Technology, Hong Kong 999077, China. [3]State Key Laboratory of Low Dimensional Quantum Physics, Department of Physics, Tsinghua University, Beijing 100084, China. [4]Frontier Science Center for Quantum Information, Beijing 100084, China. [5]Collaborative Innovation Center of Quantum Matter, Beijing 100084, China. [6]Department of Physics and Astronomy, University of Tennessee, Knoxville, TN 37996, USA. [7]Min H. Kao Department of Electrical Engineering and Computer Science, University of Tennessee, Knoxville, TN 37996, USA.
*Corresponding author. Email: songcheng@mail.tsinghua.edu.cn (C.S.); liuj@ust.hk (J.L.); panf@mail.tsinghua.edu.cn (F.P.)
†These authors contributed equally to this work.

read out by the anomalous Hall effect (AHE) (28–31) in some recently found special cAFMs with spin-splitting band structure (32–37), also termed as altermagnets (38, 39). Moreover, their spin-splitting band structure and related properties, such as unconventional spin current generation (40–42) and piezomagnetism (37), can all be manipulated through 180° switching of the Néel vector, which makes it very promising to investigate the electrical 180° switching of Néel vector in spin-splitting AFM.

Here, we achieve deterministic electrical 180° switching of the Néel vector in spin-splitting AFM Mn_5Si_3 films based on SOTs with asymmetric switching barrier that can be easily generalized to other AFM materials. We prove theoretically and experimentally that 180° switching of the Néel vector indeed tunes the spin-splitting bands and flips the anomalous Hall conductivity (AHC), which can be used as an unconventional electrical readout approach of 180° switching. With these write and read methods ready, we successfully fabricate an AFM device with high and low resistance that realizes robust write and readout cycles, paving the way for the long-desired electrical-controllable AFM-RAM.

RESULTS

Spin splitting manipulated by reversing the Néel vector

We start with introducing basic crystal structure and magnetic phase characteristics of Mn_5Si_3. The space group of Mn_5Si_3 at room temperature is $P6_3/mcm$ with the unit cell composing of four Mn_a and six Mn_b atoms at two inequivalent Wyckoff positions and six Si atoms (Fig. 1A) (43–45). As temperature decreases, Mn_5Si_3 undergoes a magnetic phase transition from paramagnetic to cAFM and then to ncAFM. In the cAFM phase, the G-type AFM ordering occurs on two-thirds of Mn_b atoms, where adjacent magnetic Mn_b atoms have opposite spin orientations to form the Néel vector (Fig. 1A and fig. S1 for other perspectives) (43–47). The PT symmetry is broken in cAFM Mn_5Si_3 thin film (29), and, hence, its energy state at a generic momentum is spin-polarized, i.e., $E_k^\uparrow \neq E_k^\downarrow$, because of the exchange coupling between itinerant electrons and local magnetic moments. Moreover, the states at mirror symmetry–related momenta must have contrasting spin polarizations to form the C-paired spin-momentum locking, further suppressing spin-flipping (37), which is confirmed by our first-principles calculations as shown in Fig. 1B. These unique features provide possibilities for the existence of AHE in cAFM Mn_5Si_3 thin film (29).

Next, it is demonstrated that through reversing the Néel vector, we can manipulate spin-resolved and Berry curvature–dependent phenomena, which, in turn, serve as potential readout approach of 180° Néel vector switching in cAFM Mn_5Si_3. Although spin-orbit coupling has negligible effect on the band structure (fig. S1), it can break the strict SU (2) symmetry and, hence, induce nonzero Berry curvature for spin-splitting bands of cAFM Mn_5Si_3 with C-paired
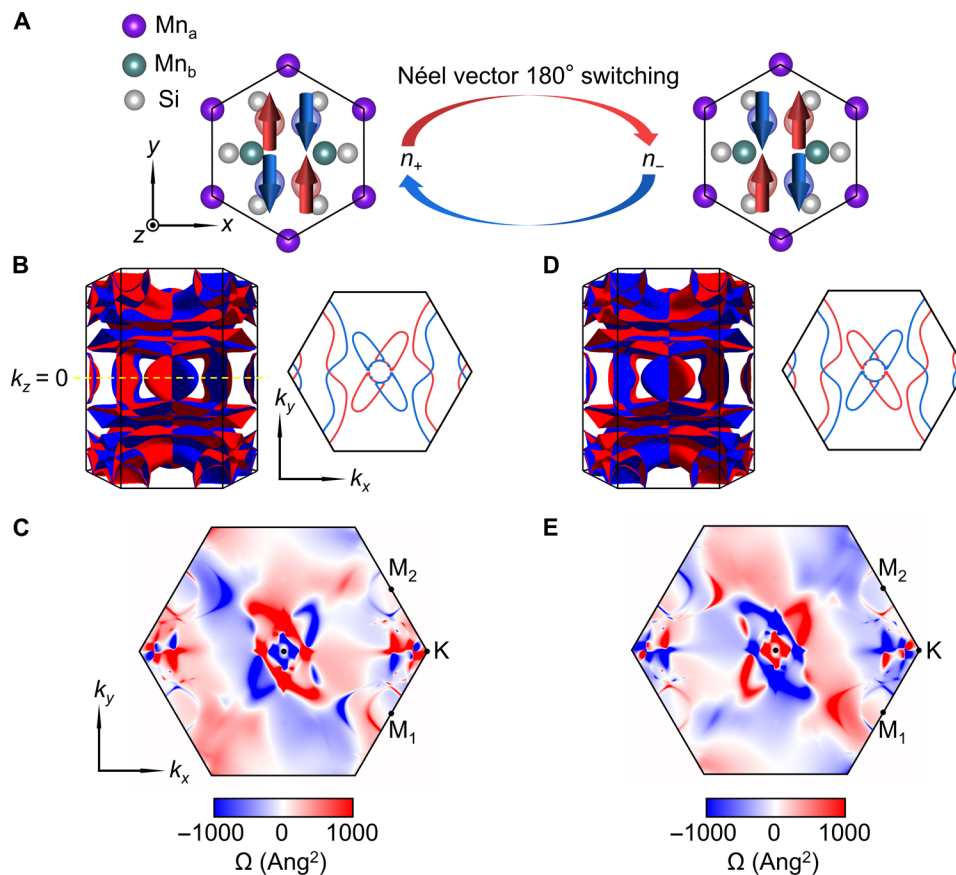

Fig. 1. Spin-splitting band and Berry curvature in Mn_5Si_3 of opposite Néel vectors. (**A**) Crystal and magnetic structure of G-type cAFM Mn_5Si_3 with opposite magnetization density represented by red and blue isosurfaces. (**B** and **D**) Fermi surface and its contour plot in the $k_z = 0$ plane. (**C** and **E**) Berry curvature in the $k_z = 0$ plane. When the Néel vector is 180°-switched, both spin-splitting band and Berry curvature are flipped.

spin-momentum locking as presented in Fig. 1C. When the Néel vector n is switched 180° from n_+ to n_-, equivalent to the time-reversal operation, the spin orientations will be reversed (Fig. 1A). Accordingly, both spin splitting (Fig. 1B) and Berry curvature (Fig. 1C) at (k_x, k_y) will switch their signs at the T-paired momentum ($-k_x$, $-k_y$), as displayed in Fig. 1 (D and E, respectively). Therefore, through 180° Néel vector switching, we can control the spin-splitting bands and Berry curvature and, hence, manipulate all spin-resolved and Berry curvature–dependent phenomena such as AHE. Correspondingly, AHE may serve as a potential readout method of 180° Néel vector switching.

Demonstration of AHE as a readout method

As expected, AHE is observed distinctly in the cAFM temperature range (60 to 230 K) of sputtered Mn_5Si_3(0001) thin films (fig. S2 and text S1) by Hall resistivity measurements (fig. S3) and polar magneto-optical Kerr effect measurements (fig. S4). Typical hysteresis of Hall resistivity ρ_{yx} under out-of-plane magnetic field at 150 K is shown in Fig. 2A, exhibiting a nonvolatile characteristic. Notably, the

corresponding hysteresis of magnetization M in Fig. 2B exhibits two abrupt changes around zero field and 4 kOe: The one around zero field (black line) is due to the net moment from unavoidable local defects in the sputtering process, which does not contribute to ρ_{yx} near zero field and can be markedly suppressed (fig. S5 and text S2). The other around 4 kOe (blue line) has consistent coercive field H_c with that of the ρ_{yx} hysteresis, which can be more clearly illustrated by similar peak locations in field-derivative hysteresis of both ρ_{yx} and M around 4 kOe (fig. S3 and text S1). The net moment around 4 kOe, denoted to be m, most likely originates from the relativistic Dzyaloshinskii-Moriya interaction (DMI) due to interfacial symmetry breaking (48).

A natural question is that whether the AHE is simply due to this net moment m. The answer is that AHE comes from Néel vector–dependent Berry curvature instead of m. First, the measured m can be as small as ~1 emu cm^{-3}, corresponding to only 2.5 mμ_B per magnetic Mn_b atom, which can hardly induce the measured large ρ_{yx} of 0.17 microhm cm with comparable magnitude to typical FMs (49, 50). m varies for samples of different thicknesses, but ρ_{yx} almost
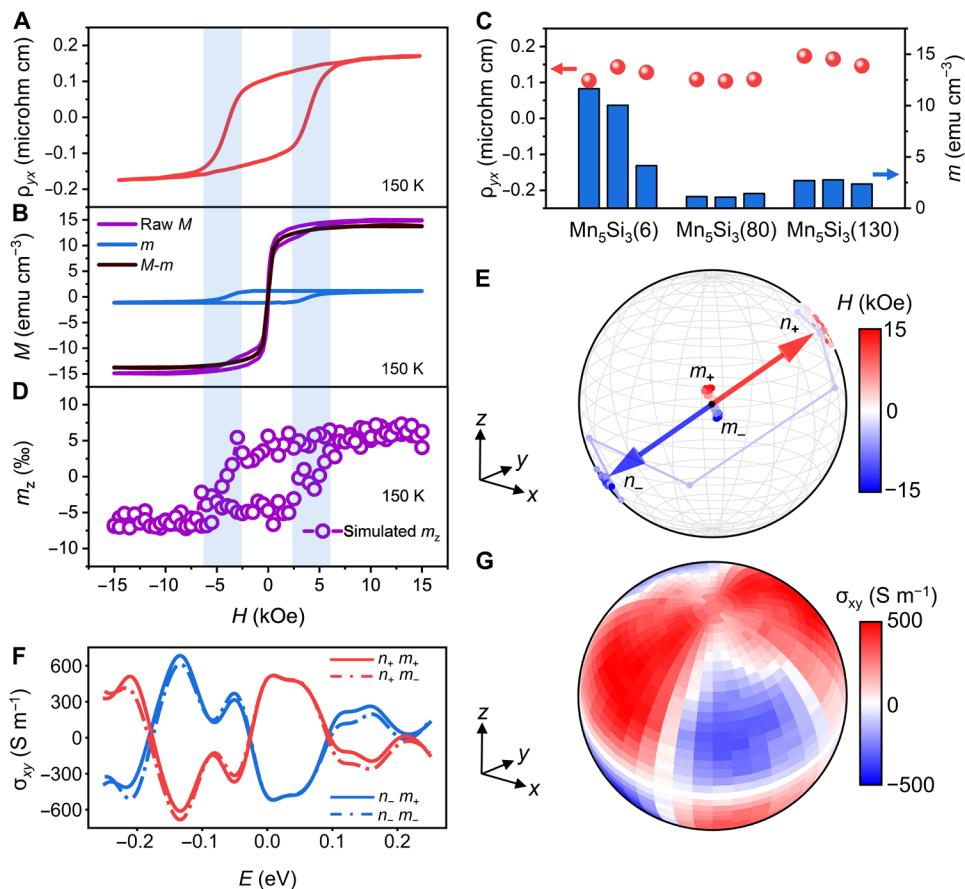

Fig. 2. Electrical detection of the Néel vector of Mn₅Si₃ by the AHE. (**A**) Hysteresis of Hall resistivity ρ_{yx} and (**B**) magnetization M under out-of-plane magnetic field at 150 K, within the cAFM phase of Mn_5Si_3. M can be decomposed into DMI-induced m as blue line and defect-induced M-m as black line. (**C**) Comparison between ρ_{yx} and m of Mn_5Si_3 thin films with different thickness at 150 K. The numbers in parentheses indicate the thickness of the film in nanometer. (**D**) Simulated hysteresis of out-of-plane net moment m_z under out-of-plane magnetic field at 150 K. (**E**) Simulated trajectories of 180° switching of Néel vector n and net moment m by out-of-plane magnetic field from 15 kOe to −15 kOe at 150 K. m and n are defined on the basis of the AFM sublattice of Mn_5Si_3 and averaged over all of simulation cells (Materials and Methods). (**F**) Calculated σ_{xy} near the Fermi level for the Néel vector along n_+ or n_- with net moment along m_+ or m_- at 150 K. (**G**) Calculated σ_{xy} at the Fermi level for n along any direction at 150 K.

remains unchanged, which further rules out that ρ_{yx} comes from m (Fig. 2C, fig. S6, and text S2). Moreover, the coercive field of AHE markedly decreases when the width of the Hall bar is reduced below 500 nm, which is quite different from FMs (fig. S7 and text S2). Besides, ρ_{yx} has opposite temperature dependence compared to longitudinal resistivity ρ_{xx} (inset of fig. S3), which excludes out extrinsic mechanisms and indicates intrinsic mechanism (*49, 50*). Hence, the experimentally observed AHE should be attributed to the intrinsic Néel vector–dependent Berry curvature as indicated by first-principles calculations in Fig. 1. Note that there is no detectable net moment m in a previous result on cAFM Mn_5Si_3 thin film, which may be due to different deposition methods and substrates (*29*). It is worth emphasizing that it is impossible to measure AHE with absolutely zero net moment because both Hall vector and magnetization follow the same symmetry rules (*31, 49, 50*).

We further performed a systematic theoretical study through atomic spin simulations and first-principles calculations (Materials and Methods) to explicitly explain why the AHE indeed arises from n-dependent Berry curvature instead of the negligible net moment m. We first demonstrate that the 180° switching of m by reversing magnetic field will simultaneously drive the Néel order n to reverse, which provides prerequisites for n-dependent AHE measured by sweeping magnetic field. It is investigated from the responses of m and n to external magnetic field by simulations, considering the realistic crystal and magnetic structure of cAFM Mn_5Si_3 with all of the parameters extracted from first-principles calculations (figs. S8 and S9 and text S3). The simulated magnetic hysteresis is shown in Fig. 2D, where the coercive field and the magnitude of simulated m match very well with experimental m in Fig. 2B (text S3). Figure 2E presents the simulated trajectories of both m and n when sweeping the out-of-plane magnetic field H from 15 to −15 kOe, where the 180° switching of m from m_+ to m_- by H drives the 180° switching of n from n_+ to n_- simultaneously. This process only requires overcoming the magnetic anisotropy energy (MAE) because m and n remain the same chirality with unchanged DMI energy. The reverse of m can also be achieved without reversing n by only switching the tilting direction of cAFM moment, which does not overcome the MAE but changes the chirality between m and n, and thus increases DMI energy. However, this scenario can be excluded for cAFM Mn_5Si_3 because simply reversing m without reversing n cannot bring about the measured AHE, as we discussed in the previous paragraph. In addition, first-principles calculations also reveal that MAE is one order of magnitude smaller than DMI energy (text S3), further illustrating that the reverse of m and n will appear simultaneously in cAFM Mn_5Si_3.

With m and n reverse at the same time demonstrated, we move on to demonstrate that it is the reverse of n instead of m that determines the AHE by first-principles calculations. The dependence of AHC σ_{xy} on both m and n in cAFM Mn_5Si_3 is calculated at 150 K, as shown in Fig. 2F. σ_{xy} at the Fermi level is calculated to be approximately 400 S m^{-1}, matching the experimentally obtained σ_{xy} of around 300 S m^{-1}. Notably, σ_{xy} values for n_+ with m_+ or m_- are almost the same, but both are opposite to those for n_- with m_+ or m_-. Thus, the influence of m on σ_{xy} is negligible, and the sign reversal of σ_{xy} is determined by the 180° switching of n, consistent with aforementioned experimental results. Moreover, σ_{xy} at the Fermi level for n along any direction is calculated and presented as a spherical image in Fig. 2G. It turns out that σ_{xy} always reverses once n is 180° switched, irrespective of any specific direction n aligning. As a result, both our experimental and theoretical results reveal that the sign of σ_{xy} is

uniquely determined by the direction of n, and thus, the AHE can serve as a reliable readout method for 180° switching of n in cAFM Mn_5Si_3.

Asymmetric energy barrier mechanism for electrical 180° switching of Néel vector

After solving the problem of reading the 180° switching of Néel vector, the remaining question is how to realize the deterministic electrical 180° switching of Néel vector, i.e., the information write process. There are three basic requirements in general: (i) Both n_+ and n_- should be stable with minimum energy to realize binary information states "0" and "1"; (ii) n needs to be driven into motion electrically; (iii) transition from n_+ to n_- and its time-reversal counterpart from n_- to n_+ must have unequal energy barriers to achieve the deterministic switching. The requirement (i) is naturally satisfied in cAFMs since both n_+ and n_- are stable along the easy axis due to MAE, and thus, we will focus on how to fulfill requirements (ii) and (iii) in the following.

According to the definition of m and n, they are always perpendicular to each other in canted AFMs, and a strong DMI vector d enforces a fixed chirality between m and n as demonstrated above in cAFM Mn_5Si_3. Without losing the generality, we start by assuming d to be perpendicular to the plane of m and n, which forms an orthogonal coordinate system as presented in Fig. 3A. To achieve requirement (ii), n needs to be driven into rotation along the $n \times p$ direction through the AFM exchange torque induced by the spin polarization p, which can be usually generated from the spin Hall effect of heavy metals such as Pt adjacent to Mn_5Si_3. We first consider p perpendicular to the plane of m and n, i.e., along d, and n will roughly rotate circularly in this plane (Fig. 3A) for this scenario. However, because of equal transition barriers of n_+ to n_- and n_- to n_+ ($H = 0$ case of Fig. 3B), n will rotate continuously driven by p and, lastly, nondeterministically relaxes to n_+ or n_- after p is withdrawn. To address this issue, we propose to construct asymmetric switching barriers through a fixed magnetic field H acting on nonzero m as shown in Fig. 3B ($H > 0$ case), and the asymmetry will be maximized when H is perpendicular to m as shown in Fig. 3A. In this case, through choosing a positive p with suitable magnitude, n can rotate from n_+ to n_- through the lower barrier but cannot further climb over the higher barrier from n_- to n_+ and thus stays at the intermediate state n'_-. When p is withdrawn, n will naturally stabilize as n_-. Similarly, by applying another p with opposite direction, n can switch from n_- back to n_+ through the same lower energy barrier. Thus, the desired deterministic 180° switching between n_+ and n_- can be electrically realized by damping-like SOT with a tiny external magnetic field.

This SOT mechanism with asymmetric energy barrier for 180° switching between n_+ and n_- can further be confirmed explicitly by atomic spin simulations. Under a positive p, n will rotate clockwise accompanied by m moving toward the hemisphere favored by positive H and then settles at an intermediate state n'_- (Fig. 3C). After SOT is turned off, n will naturally relax to the local energy minimum n_- to achieve the deterministic 180° switching from n_+ to n_- (fig. S10 for other perspectives). Similarly, n will switch back to n_+ from n_- deterministically with a reversing p through anticlockwise rotation (Fig. 3D). Reversing the direction of H also gives rise to deterministic 180° switching with reversing switching polarity (fig. S11). The same conclusion can be drawn through similar mechanisms for arbitrary orientations of p and H revealed by atomic spin simulations, even when d is not perpendicular to m and n (text S4 and figs. S12 and
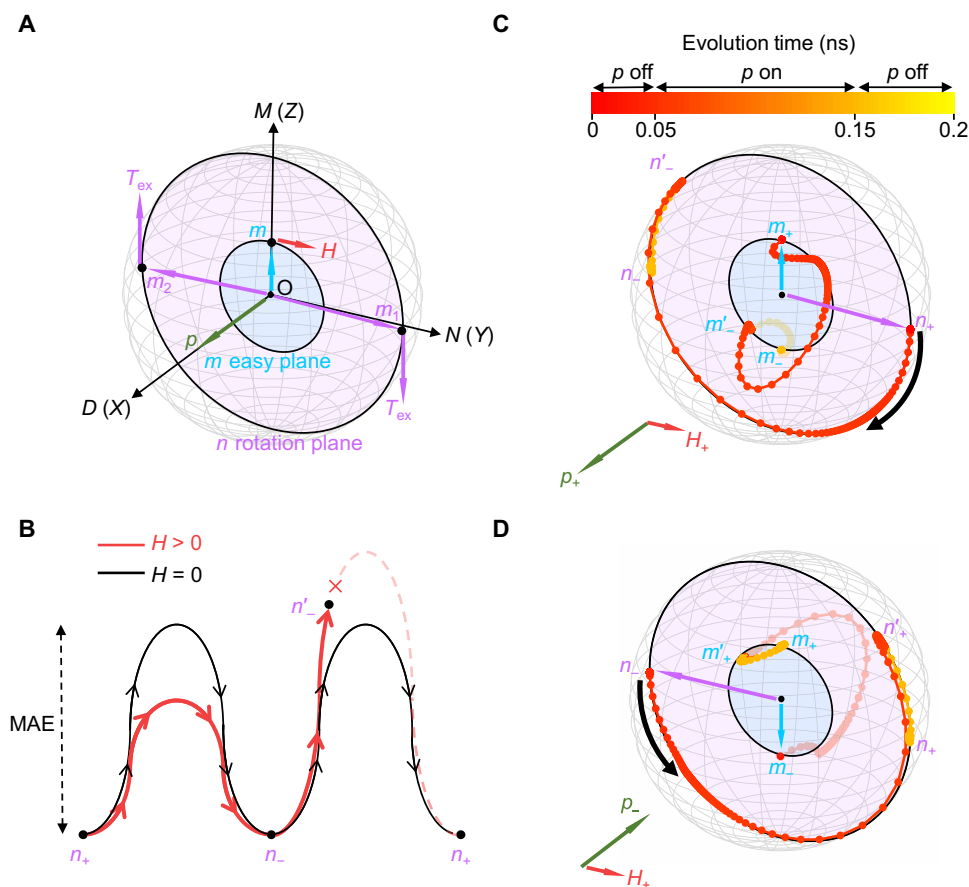
Fig. 3. Mechanism for 180° switching of the Néel vector by SOT. (**A**) Schematic of n rotation driven by exchange torques T_{ex} with p along $+X$ and n along $+Y$. n can be simplified as $(m_1 - m_2)/2$ for cAFM Mn$_5$Si$_3$ with four sublattices where $m_1 = m_3$ and $m_2 = m_4$ (Materials and Methods). Damping-like SOT shares the same direction for m_1 and m_2 on opposite AFM sublattice as $T_{DL} \sim m_1 \times (p \times m_1) \sim m_2 \times (p \times m_2)$. Hence, T_{DL} pulls m_1 and m_2 toward the direction of p, bringing about exchange torques $T_{ex} \sim m_1 \times H_{ex} \sim m_2 \times H_{ex}$ due to the AFM exchange field H_{ex}, which alters on m_1 and m_2 to drive both m_1 and m_2 to rotate coherently. The rotation of n is accompanied by the motion of m, which is favorite by magnetic field H along $+Y$. (**B**) Schematic of energy barriers for the transition from n_+ to n_- and n_- to n_+. Without H, these two energy barriers are the same, determined by MAE. With nonzero H such as $H > 0$, the degeneracy between them cannot be maintained. (**C**) Simulated switching trajectories of m and n for positive p_+ and positive H_+ as well as (**D**) negative p_- and positive H_+. m is magnified 10 times for better visualization. The color of trajectories indicates the evolution time, where p is added from 0.05 ns to 0.15 ns.

S13). Note that this mechanism is not restricted to Mn$_5$Si$_3$ but can be easily generalized to other AFMs with tiny intrinsic net moment.

Experimental demonstration of electrical 180° switching of the Néel vector

We carried out SOT switching experiments on Mn$_5$Si$_3$(0001)/Pt crossbars of 6 μm by 4 μm (Fig. 4A) based on the mechanism above, where Pt serves as the spin source. Electrical pulses of different magnitude were introduced into the write channel WI$^+$-WI$^-$ with an assistant field H along the same direction, and the Hall voltage was collected simultaneously along RI$^+$-RI$^-$ to read the direction of n through AHE. As expected, 180° switching of n in cAFM Mn$_5$Si$_3$ are observed under various temperatures (fig. S14), and the results at 180 K are representatively presented in Fig. 4B. The largest switching ratio reaches 41%, and such an incomplete switching is most likely due to the existence of microscopical multidomain and local defects pinning (fig. S15). Opposite switching polarity can be observed if the polarity of current pulse or H is reversed, consistent with

aforementioned theoretical results and matching basic symmetry requirements for deterministic SOT switching (*9*, *10*). No switching can be observed with a high H of 8 kOe, which confines the direction of m and thus also confines the direction of n, further verifying that the change of Hall voltage is due to the switching of n instead of thermal artifacts. Moreover, AHE can also be observed in the temperature range of ncAFM Mn$_5$Si$_3$ (below 60 K), but electrical 180° switching cannot be achieved, further demonstrating that it is n that can be switched electrically (fig. S16).

We now show that the 180° SOT switching of n in cAFM Mn$_5$Si$_3$ is fundamentally different from FMs and ncAFMs such as Mn$_3$Sn (*26*, *27*, *51*–*55*). In FMs, the assistant field H can effectively assist the SOT to overcome MAE for switching, as characterized by a linear decrease of the critical switching current density J_c with increasing H (*44*). In contrast, for cAFM Mn$_5$Si$_3$, H only eliminates the degeneracy of energy barriers between n_+ to n_- and n_- to n_+ but barely helps n to overcome MAE. That is because it is the large AFM exchange energy that determines the tilting of n toward p as a prerequisite to obtain
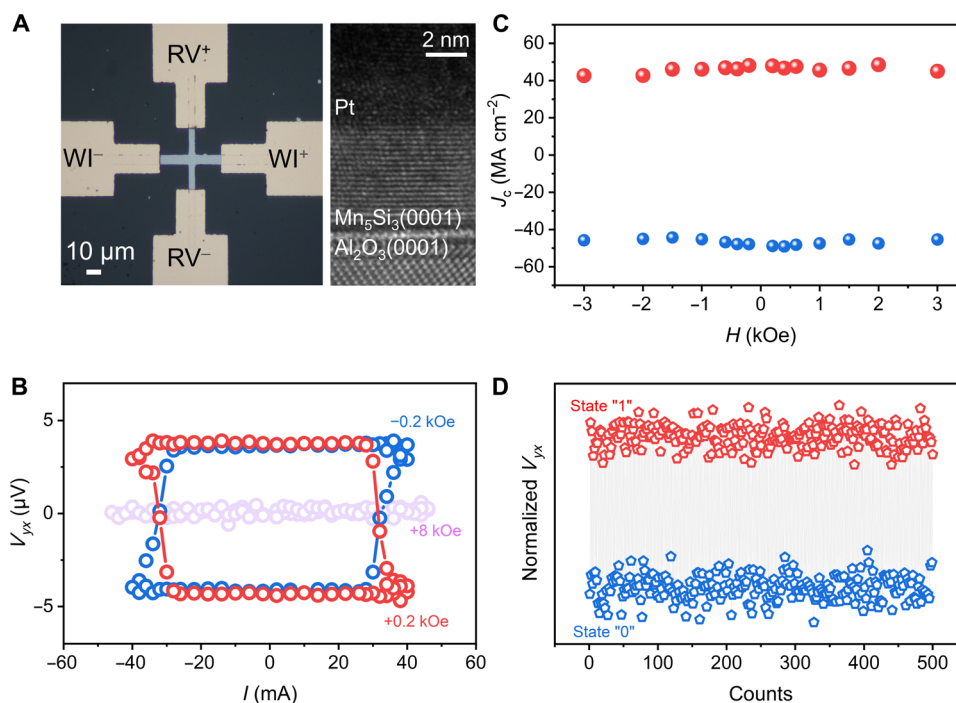
Fig. 4. Electrical 180° switching of the Néel vector of Mn$_5$Si$_3$. (**A**) Optical microscopy and transmission electron microscopy image of Mn$_5$Si$_3$(0001)/Pt crossbars for electrical switching. WI$^+$ and WI$^-$ denote the write channel where the electrical pulse I is added, and RV$^+$ and RV$^-$ denote the read channel where the Hall voltage V_{yx} is collected. (**B**) Hall voltage V_{yx} as a function of electrical pulse I for different H of −0.2, 0.2, and 8 kOe at 180 K. (**C**) Critical switching current density J_c under different assistant field H at 180 K. (**D**) Continuous cycling between high V_{yx} (state "1") and low V_{yx} (state "0") by 180° switching of n for 500 electrical pulses at 180 K.

nonzero AFM exchange torque for overcoming MAE, where AFM exchange energy is much larger than the Zeeman energy induced by H acting on the negligible m. Thus, J_c should be very insensitive to H for cAFM Mn$_5$Si$_3$. As presented in Fig. 4C and fig. S17, we carried out SOT switching measurements under different assistant field H, and the experimentally extracted J_c (text S5) remains almost unchanged with the increase of H for cAFM Mn$_5$Si$_3$. Besides, unlike uniaxial Néel vector n as order parameter perpendicular to m in cAFM Mn$_5$Si$_3$, cluster magnetic octuple as the order parameter with complex magnetic anisotropy in ncAFM Mn$_3$Sn is parallel to its intrinsic m, leading to different dynamic behaviors under p and H of specific symmetry (*26, 27, 51–53*).

To investigate the efficiency for 180° switching of n in cAFM Mn$_5$Si$_3$, we calculate the ratio of AHE coercivity to critical switching current density $\mu_0 H_c/J_c$ as a figure of merit (*52*). For the averaged J_c of 49 MA cm^{-2} at 180 K (fig. S15), it turns out to be about 5 mT cm^2 MA^{-1}, which is five times higher than traditional ferromagnetic systems such as Pt/Co/AlO$_x$ of approximately 1 mT cm^2 MA^{-1} (*52, 56*), indicating that the 180° SOT switching of n in cAFM Mn$_5$Si$_3$ shows high efficiency. Moreover, we test the endurance for 180° switching of n by applying electrical pulses with opposite directions alternately. The Hall voltage can be switched between high and low values corresponding to information states between "0" and "1" (Fig. 4D), which is reversible and reproducible. The device does not show degradation after 500 cycles, manifesting its robustness. As a result, spin-splitting Mn$_5$Si$_3$ shows unique advantages to construct electrical-controllable AFM-RAM with low power consumption, high reliability, and exceptional abundance in addition to its intrinsic high density and high speed.

DISCUSSION
We achieve electrical 180° switching of the Néel vector in spin-splitting cAFM Mn$_5$Si$_3$. The demonstration of electrical 180° switching of the Néel vector involves two steps. One is to prove that it is the 180° switching of the Néel vector instead of net moment that tunes the spin-splitting band structure and brings about opposite AHC, which makes AHE as a unique readout method of 180° switching of Néel vector. It is supported by both systematic theoretical calculations and several control experiments including thickness-dependent and channel width–dependent measurements. The other is to design SOT switching mechanism with asymmetric energy barriers between n_+ and n_-. It is experimentally implemented and confirmed by realizing current and assistant field polarity–dependent 180° Néel vector switching and further verified by assistant field magnitude-dependent measurements and nonswitching of ncAFM Mn$_3$Sn. On the basis of electrical 180° switching and electrical readout of the Néel vector in Mn$_5$Si$_3$, electrical-controllable AFM devices with "0" and "1" resistance states were fabricated, which show high efficiency and high reproducibility. Our results establish the groundwork for practical applications of spin-splitting AFMs in next-generation information technology and serve as the basis of exploring other intriguing properties in spin-splitting AFMs arising from interactions among different degrees of freedom such as spin, valley, and charge.

MATERIALS AND METHODS
Sample preparation
Six nanometers of Mn$_5$Si$_3$(0001) films was grown on Al$_2$O$_3$(0001) substrates by cosputtering of Mn and Si at 465°C with a rate of 0.4 Å s^{-1} under a base pressure below 5×10^{-8} torr, followed by annealing at

600°C for 2 hours. After that, 10-nm Pt was deposited in situ by magnetron sputtering at room temperature. Crossbars (6 μm by 4 μm) for SOT switching measurements were patterned using optical lithography combined with Ar ion milling. Then, Cr(10 nm)/Cu(70 nm) electrode was electron beam (e-beam)–evaporated for wire bonding. For room temperature and low-temperature x-ray diffraction (XRD) measurements, $Mn_5Si_3(0001)$ films (80 nm) were prepared to obtain diffraction peaks with substantial intensity for precisely determining the lattice parameter. Besides, $Mn_5Si_3(0001)$ films (130 nm) were grown for control measurements. For size-dependent measurements of the AHE, e-beam lithography was used to fabricate crossbars with width varying from 100 nm to 5 μm. All of the samples were kept in a glove box with O_2 and $H_2O < 0.01$ parts per million to prevent degradation or oxidation.

Characterizations

Cross-sectional transmission electron microscopy (TEM) images for $Mn_5Si_3(6\ nm)/Pt(10\ nm)$ were collected at room temperature using a commercial TEM system (JEM-2100F). Magnetic hysteresis curves were collected in commercial superconducting quantum interference device (SQUID; Quantum Design), where the diamagnetic contribution of $Al_2O_3(0001)$ substrate was subtracted. Magnetization-temperature curves were also collected from SQUID without subtracting diamagnetic contribution of $Al_2O_3(0001)$ substrate. θ-2θ XRD measurement at room temperature was carried out at Rigaku SmartLab. In situ θ-2θ XRD at low temperatures was performed at BL02U2 Beamline from Shanghai Synchrotron Radiation Facility. Atomic force microscopy images were collected at Bruker Dimension FastScan.

Transport measurements

$ρ_{xx}$ and $ρ_{yx}$ of Mn_5Si_3 films were measured using a standard four-terminal method in commercial Physical Property Measurement System (Quantum Design). Ordinary Hall resistivity that is linear to magnetic field was subtracted from $ρ_{yx}$. For SOT switching measurements, writing pulses (1 ms) within the range of 46 mA were added in the WI^+-WI^- channel with an assistant field H applied along the WI^+-WI^- channel, followed by waiting for 10 s before collecting the Hall voltage in the RV^+-RV^- channel by a nanovoltmeter with a base current of 2 mA (Fig. 4A).

Time-resolved reflectivity measurements

Time-resolved reflectivity measurements were carried out by a Ti:sapphire oscillator (center wavelength of 800 nm, repetition rate of 80 MHz, and pulse width of 20 fs) in a typical wavelength-degenerate pump-probe setup. Both the pump and probe beams were linearly polarized in a cross-polarization configuration to block the pump scattering. The pump beam was focused to 30 μm on the sample with a fixed fluence at 35.4 μJ/cm^2. The focal spot size and fluence of the probe beam were about 2 and 40 times smaller than those of the pump beam, respectively. The intensity of the pump beam was modulated by an optical chopper at 3 kHz to facilitate lock-in detection. The reflectivity signal was detected by a balanced detector to suppress laser power fluctuations. The sample was kept in a cryostat under vacuum of better than 1×10^{-3} mbar during experiments.

Magneto-optical Kerr effect measurements

The polar magneto-optical Kerr effect measurements were carried out using a power-stabilized 633-nm HeNe laser. After transmitting through a linear polarizer, the light (25 μW) was focused to an ~1-μm spot on the sample by a 40× reflective objective at normal incidence to avoid the large backgrounds that occur when a typical lens is used. The sample was mounted in the vacuum chamber of an optical superconducting magnet system with the magnetic field applied perpendicular to the sample plane (Faraday geometry). The reflected beam was modulated at ~50 kHz by a photoelastic modulator, split by a Wollaston prism and detected using a balanced photodiode with a standard optical bridge arrangement. The resulting 50- and 100-kHz modulations detected by lock-in amplifiers then correspond to the ellipticity and rotation angle of the beam, respectively. We additionally modulated the intensity of the beam with a lower-frequency (~1319 Hz) chopper to measure the dc signal for normalization using a third lock-in amplifier. The background from the optic window and a linear background were subtracted.

First-principles calculations

First-principles calculations were performed on the basis of density functional theory (DFT) (57) as implemented in Vienna ab initio simulation package (58). Exchange-correlation interaction was described by the Perdew-Burke-Ernzerhof parametrization of generalized gradient approximation (59). We also used Perdew-Wang (60) and local density approximation exchange-correlation functional, where similar results were obtained. Structures were relaxed until the force on each atom is less than 0.01 eV/Å. The cutoff energy and electronic iteration convergence criterion were set to 400 and 10^{-5} eV, respectively. To model the Brillouin zone, a Monkhorst-Pack (MP) k-grid mesh (61) of $7 \times 7 \times 9$ was used. For MAE calculations, self-consistent charge density was read to get a converged result. Four-states method was used to evaluate the strength of DMI. Berry curvature and AHC were calculated on the basis of ab initio tight-binding models with all parameters extracted from first-principles calculations using the FPLO software (62).

Atomic spin simulations of magnetic hysteresis

We carried out atomic spin simulations on VAMPIRE software (63), which can define specific lattice parameters a and c consistent with our hexagonal cAFM phase Mn_5Si_3 thin film of 6.902 and 4.795 Å, respectively. Discretized $50 \times 50 \times 10$ units cells in the x-y-z direction were used to model the Mn_5Si_3 thin film. The Hamiltonian of the system at 0 K can be written as following

$$H_{total} = \sum_{<ip,jq>} J_{ip,jq} m_{ip} \cdot m_{jq} + \sum_{<ip,jq>} d_{ip,jq} \cdot (m_{ip} \times m_{jq}) - K \sum_{ip} (k \cdot m_{ip})^2 + H_Z$$

Here, i and j denote unit cell and p and q represent sublattice (p, $q = 1, 2, 3, 4$). H_{total} is the total Hamiltonian, and m_{ip} (m_{jq}) is the unit magnetic moment at sublattice Mn_p (Mn_q) of unit cell i (j) with the magnitude of 2.4 μB. $J_{ip,jq}$, $d_{ip,jq}$, and K are the exchange interaction constant, the DMI vector, and the uniaxial anisotropy constant, respectively. H_Z is the Zeeman energy under magnetic field, equaling $-μ_0 m_s \sum_{ip} m_{ip} \cdot H$, where $μ_0$, m_s, and H are the vacuum permeability, the saturation magnetization of magnetic Mn atom, and the external field, respectively. k is the direction of easy axis, which was set to be (1,1,1) direction in the cartesian coordinate system with the uniaxial anisotropy constant K of 0.1 meV from DFT estimations (text S3). Four exchange interactions were considered, namely $J_1 = -12.23$ meV, $J_2 = -2.16$ meV, $J_3 = 3.98$ meV, and $J_4 = 2.89$ meV (fig. S8A) with magnitude consistent with former DFT calculation results (64, 65).

Note that J_4 interaction was set to be ferromagnetic to eliminate the $t\mathscr{T}$ symmetry for consistency with experimentally measured nonzero σ_{xy} (text S3). The DMI vector was set along x axis with a magnitude of 1.35 meV from DFT calculations and the experimentally measured out-of-plane AHE-related net moment m (text S2). These settings of basic material parameters give a simulated magnetic hysteresis that is analogous with SQUID-derived m under 150 K (Fig. 2C and text S2), illustrating that these parameters are suitable for modeling the magnetic switching behavior of cAFM Mn_5Si_3. Specifically speaking, the Landau-lifshitz-Gilbert (LLG) equation for each magnetic Mn atom is written as

$$\frac{dm_{ip}}{dt} = -|\gamma| m_{ip} \times H_{\text{eff},ip} + \alpha m_{ip} \times \frac{dm_{ip}}{dt}$$

where $H_{\text{eff},ip}$ is the effective magnetic field acting on the magnetic Mn atom at sublattice p of unit cell i. $H_{\text{eff},ip} = -\frac{\partial H_{\text{total}}}{\partial m_{ip}} + H_{\text{th}.ip}$, where $H_{\text{th},ip}$ is the Gaussian stochastic magnetic field to describe the effect of finite temperature (66). γ and α are the gyromagnetic ratio of the electron and the Gilbert damping coefficient, equaling 176 s^{-1} T^{-1} and 0.1, respectively. A fine iteration time step Δt of 0.1 fs was used to precisely capture the dynamics of atomic magnetic moments. First, the system was initialized with random orientations of atomic magnetic moments and then relaxed into a perfect G-type AFM ordering at 0 K (fig. S8B). After applying negative magnetic field, each atomic magnetic moment can be switched by 180° (fig. S8C). The simulated m and n for each unit cell should be defined as $m = (m_1 + m_2 + m_3 + m_4)/4$ and $n = (m_1 - m_2 + m_3 - m_4)/4$, which further equaling $(m_1 + m_2)/2$ and $(m_1 - m_2)/2$ because $m_1 = m_3$ and $m_2 = m_4$ due to J_3. Thus, the 180° switching of each atomic magnetic moment is consistent with the 180° switching of m and n. Then, the hysteresis was simulated at 150 K (Fig. 2D), and 180° switching of m and n can also be observed (Fig. 2E), where m and n on all of unit cells were averaged.

Atomic spin simulations of SOT switching

To understand the mechanism for SOT 180° switching of the Néel vector n of cAFM Mn_5Si_3, we consider the damping-like effective field H_{DL} of the spin polarization p generated by the spin Hall effect of Pt. Then, the LLG equation under SOT can be written as

$$\frac{dm_{ip}}{dt} = -|\gamma| m_{ip} \times H_{\text{eff},ip} + \alpha m_{ip} \times \frac{dm_{ip}}{dt} + \xi_{\text{DL}} m_{ip} \times (p \times m_{ip})$$

$$= -|\gamma| m_{ip} \times H_{\text{eff},ip} + \alpha m_{ip} \times \frac{dm_{ip}}{dt} + |\gamma| m_{ip} \times H_{\text{DL},ip}$$

where $H_{\text{DL},ip}$ is the damping-like effective field of SOT acting on the magnetic Mn atom at sublattice p ($p = 1, 2, 3, 4$) of unit cell i. p is the unit vector for the spin polarization. ξ_{DL} is the magnitude of damping-like SOT, which has linear relationship with the magnitude of $H_{\text{DL},ip}$ and current density J (text S3). Note that for the simulation of SOT switching, $5 \times 5 \times 5$ unit cells were used to save calculation time, which gives consistent results with that of $50 \times 50 \times 10$ unit cells. In analogous to the simulations for magnetic hysteresis, the system was initialized with random orientations of atomic magnetic moments and relaxed into G-type AFM ordering before adding a 0.1-ns-long electrical pulse with transverse p under assistant field H. The magnitude of assistant field H was fixed at 10 kOe. This magnitude of H is reasonable because the simulations of SOT switching were carried out

at 0 K, and the coercive field of simulated magnetic hysteresis at 0 K is around 150 kOe. It means that H of no more than 10% of the coercive field can assist the deterministic 180° switching of n, consistent with experimental results. m and n on all of unit cells were averaged to plot trajectories of m and n under p. The settings of pulse lengths and random seeds do not influence simulation results, proving their reliability (text S6). The influence of field-like SOTs was also investigated by adding field-like effective field H_{FL} as a term of $|\gamma| m_{ip} \times H_{\text{FL},ip}$. It turns out that H_{FL} has a negative influence on SOT switching, which increases the critical switching current density (text S7).

Supplementary Materials

This PDF file includes:
Texts S1 to S7
Figs. S1 to S20
Legend for movie S1
References

Other Supplementary Material for this manuscript includes the following:
Movie S1

REFERENCES AND NOTES

1. S. A. Wolf, D. D. Awschalom, R. A. Buhrman, J. M. Daughton, S. von Molnár, M. L. Roukes, A. Y. Chtchelkanova, D. M. Treger, Spintronics: A spin-based electronics vision for the future. *Science* **294**, 1488–1495 (2001).

2. S. Bhatti, R. Sbiaa, A. Hirohata, H. Ohno, S. Fukami, S. N. Piramanayagam, Spintronics based random access memory: A review. *Mater. Today* **20**, 530–548 (2017).

3. C. Song, R. Q. Zhang, L. Y. Liao, Y. J. Zhou, X. F. Zhou, R. Y. Chen, Y. F. You, X. Z. Chen, F. Pan, Spin-orbit torques: Materials, mechanisms, performances, and potential applications. *Prog. Mater. Sci.* **118**, 100761 (2021).

4. M. Julliere, Tunneling between ferromagnetic films. *Phys. Lett.* **54**, 225–226 (1975).

5. T. Miyazaki, N. Tezuka, Giant magnetic tunneling effect in Fe/Al₂O₃/Fe junction. *J. Magn. Magn. Mater.* **139**, L231–L234 (1995).

6. J. S. Moodera, L. R. Kinder, T. M. Wong, R. Meservey, Large magnetoresistance at room temperature in ferromagnetic thin film tunnel junctions. *Phys. Rev. Lett.* **74**, 3273–3276 (1995).

7. J. C. Slonczewski, Current-driven excitation of magnetic multilayers. *J. Magn. Magn. Mater.* **159**, L1–L7 (1996).

8. L. Berger, Emission of spin waves by a magnetic multilayer traversed by a current. *Phys. Rev. B* **54**, 9353–9358 (1996).

9. I. M. Miron, K. Garello, G. Gaudin, P.-J. Zermatten, M. V. Costache, S. Auffret, S. Bandiera, B. Rodmacq, A. Schuhl, P. Gambardella, Perpendicular switching of a single ferromagnetic layer induced by in-plane current injection. *Nature* **476**, 189–193 (2011).

10. L. Liu, C.-F. Pai, Y. Li, H. W. Tseng, D. C. Ralph, R. A. Buhrman, Spin-torque switching with the giant spin Hall effect of tantalum. *Science* **336**, 555–558 (2012).

11. T. Jungwirth, X. Marti, P. Wadley, J. Wunderlich, Antiferromagnetic spintronics. *Nat. Nanotechnol.* **11**, 231–241 (2016).

12. V. Baltz, A. Manchon, M. Tsoi, T. Moriyama, T. Ono, Y. Tserkovnyak, Antiferromagnetic spintronics. *Rev. Mod. Phys.* **90**, (2018).

13. P. Wadley, B. Howells, J. Zelezny, C. Andrews, V. Hills, R. P. Campion, V. Novak, K. Olejnik, F. Maccherozzi, S. S. Dhesi, S. Y. Martin, T. Wagner, J. Wunderlich, F. Freimuth, Y. Mokrousov, J. Kunes, J. S. Chauhan, M. J. Grzybowski, A. W. Rushforth, K. W. Edmonds, B. L. Gallagher, T. Jungwirth, Electrical switching of an antiferromagnet. *Science* **351**, 587–590 (2016).

14. P. Vaidya, S. A. Morley, J. van Tol, Y. Liu, R. Cheng, A. Brataas, D. Lederman, E. del Barco, Subterahertz spin pumping from an insulating antiferromagnet. *Science* **368**, 160–165 (2020).

15. B. G. Park, J. Wunderlich, X. Martí, V. Holý, Y. Kurosaki, M. Yamada, H. Yamamoto, A. Nishide, J. Hayakawa, H. Takahashi, A. B. Shick, T. Jungwirth, A spin-valve-like magnetoresistance of an antiferromagnet-based tunnel junction. *Nat. Mater.* **10**, 347–351 (2011).

16. Y. Y. Wang, C. Song, B. Cui, G. Y. Wang, F. Zeng, F. Pan, Room-temperature perpendicular exchange coupling and tunneling anisotropic magnetoresistance in an antiferromagnet-based tunnel junction. *Phys. Rev. Lett.* **109**, 137201 (2012).

17. X. Marti, I. Fina, C. Frontera, J. Liu, P. Wadley, Q. He, R. J. Paull, J. D. Clarkson, J. Kudrnovský, I. Turek, J. Kuneš, D. Yi, J. H. Chu, C. T. Nelson, L. You, E. Arenholz, S. Salahuddin, J. Fontcuberta, T. Jungwirth, R. Ramesh, Room-temperature antiferromagnetic memory resistor. *Nat. Mater.* **13**, 367–374 (2014).

18. D.-F. Shao, S.-H. Zhang, M. Li, C.-B. Eom, E. Y. Tsymbal, Spin-neutral currents for spintronics. *Nat. Commun.* **12**, 7061 (2021).

19. L. Šmejkal, A. B. Hellenes, R. González-Hernández, J. Sinova, T. Jungwirth, Giant and tunneling magnetoresistance in unconventional collinear antiferromagnets with nonrelativistic spin-momentum coupling. *Phys. Rev. X* **12**, 011028 (2022).

20. P. Qin, H. Yan, X. Wang, H. Chen, Z. Meng, J. Dong, M. Zhu, J. Cai, Z. Feng, X. Zhou, L. Liu, T. Zhang, Z. Zeng, J. Zhang, C. Jiang, Z. Liu, Room-temperature magnetoresistance in an all-antiferromagnetic tunnel junction. *Nature* **613**, 485–489 (2023).

21. X. Chen, T. Higo, K. Tanaka, T. Nomoto, H. Tsai, H. Idzuchi, M. Shiga, S. Sakamoto, R. Ando, H. Kosaki, T. Matsuo, D. Nishio-Hamane, R. Arita, S. Miwa, S. Nakatsuji, Octupole-driven magnetoresistance in an antiferromagnetic tunnel junction. *Nature* **613**, 490–495 (2023).

22. S. Y. Bodnar, L. Smejkal, I. Turek, T. Jungwirth, O. Gomonay, J. Sinova, A. A. Sapozhnik, H. J. Elmers, M. Klaui, M. Jourdan, Writing and reading antiferromagnetic Mn_2Au by Néel spin-orbit torques and large anisotropic magnetoresistance. *Nat. Commun.* **9**, 348 (2018).

23. X. Z. Chen, R. Zarzuela, J. Zhang, C. Song, X. F. Zhou, G. Y. Shi, F. Li, H. A. Zhou, W. J. Jiang, F. Pan, Y. Tserkovnyak, Antidamping-torque-induced switching in biaxial antiferromagnetic insulators. *Phys. Rev. Lett.* **120**, 207204 (2018).

24. Y. Cheng, S. Yu, M. Zhu, J. Hwang, F. Yang, Electrical switching of tristate antiferromagnetic Néel order in α–Fe2O3 epitaxial films. *Phys. Rev. Lett.* **124**, 027202 (2020).

25. J. Godinho, H. Reichlova, D. Kriegner, V. Novak, K. Olejnik, Z. Kaspar, Z. Soban, P. Wadley, R. P. Campion, R. M. Otxoa, P. E. Roy, J. Zelezny, T. Jungwirth, J. Wunderlich, Electrically induced and detected Néel vector reversal in a collinear antiferromagnet. *Nat. Commun.* **9**, 4686 (2018).

26. T. Higo, K. Kondou, T. Nomoto, M. Shiga, S. Sakamoto, X. Chen, D. Nishio-Hamane, R. Arita, Y. Otani, S. Miwa, S. Nakatsuji, Perpendicular full switching of chiral antiferromagnetic order by current. *Nature* **607**, 474–479 (2022).

27. J.-Y. Yoon, P. Zhang, C.-T. Chou, Y. Takeuchi, T. Uchimura, J. T. Hou, J. Han, S. Kanai, H. Ohno, S. Fukami, L. Liu, Handedness anomaly in a non-collinear antiferromagnet under spin–orbit torque. *Nat. Mater.* **22**, 1106–1113 (2023).

28. Z. Feng, X. Zhou, L. Šmejkal, L. Wu, Z. Zhu, H. Guo, R. González-Hernández, X. Wang, H. Yan, P. Qin, X. Zhang, H. Wu, H. Chen, Z. Meng, L. Liu, Z. Xia, J. Sinova, T. Jungwirth, Z. Liu, An anomalous Hall effect in altermagnetic ruthenium dioxide. *Nat. Electron.* **5**, 735–743 (2022).

29. I. Kounta, H. Reichlova, D. Kriegner, R. Lopes Seeger, A. Bad'ura, M. Leiviska, A. Boussadi, V. Heresanu, S. Bertaina, M. Petit, E. Schmoranzerova, L. Smejkal, J. Sinova, T. Jungwirth, V. Baltz, S. T. B. Goennenwein, L. Michez, Competitive actions of MnSi in the epitaxial growth of Mn5Si3 thin films on Si(111). *Phys. Rev. Mater.* **7**, 024416 (2023).

30. R. D. Gonzalez Betancourt, J. Zubac, R. Gonzalez-Hernandez, K. Geishendorf, Z. Soban, G. Springholz, K. Olejnik, L. Smejkal, J. Sinova, T. Jungwirth, S. T. B. Goennenwein, A. Thomas, H. Reichlova, J. Zelezny, D. Kriegner, Spontaneous anomalous Hall effect arising from an unconventional compensated magnetic phase in a semiconductor. *Phys. Rev. Lett.* **130**, 036702 (2023).

31. L. Šmejkal, A. H. MacDonald, J. Sinova, S. Nakatsuji, T. Jungwirth, Anomalous Hall antiferromagnets. *Nat. Rev. Mater.* **7**, 482–496 (2022).

32. L. Šmejkal, R. González-Hernández, T. Jungwirth, J. Sinova, Crystal time-reversal symmetry breaking and spontaneous Hall effect in collinear antiferromagnets. *Sci. Adv.* **6**, eaaz8809 (2020).

33. M. Naka, S. Hayami, H. Kusunose, Y. Yanagi, Y. Motome, H. Seo, Spin current generation in organic antiferromagnets. *Nat. Commun.* **10**, 4305 (2019).

34. K.-H. Ahn, A. Hariki, K.-W. Lee, J. Kuneš, Antiferromagnetism inRuO2asd-wave pomeranchuk instability. *Phys. Rev. B* **99**, 184432 (2019).

35. L.-D. Yuan, Z. Wang, J.-W. Luo, E. I. Rashba, A. Zunger, Giant momentum-dependent spin splitting in centrosymmetric low-Z antiferromagnets. *Phys. Rev. B* **102**, 014422 (2020).

36. R. Gonzalez-Hernandez, L. Smejkal, K. Vyborny, Y. Yahagi, J. Sinova, T. Jungwirth, J. Zelezny, Efficient electrical spin splitter based on nonrelativistic collinear antiferromagnetism. *Phys. Rev. Lett.* **126**, 127701 (2021).

37. H. Y. Ma, M. Hu, N. Li, J. Liu, W. Yao, J. F. Jia, J. Liu, Multifunctional antiferromagnetic materials with giant piezomagnetism and noncollinear spin current. *Nat. Commun.* **12**, 2846 (2021).

38. L. Šmejkal, J. Sinova, T. Jungwirth, Beyond conventional ferromagnetism and antiferromagnetism: A phase with nonrelativistic spin and crystal rotation symmetry. *Phys. Rev. X* **12**, 031042 (2022).

39. L. Šmejkal, J. Sinova, T. Jungwirth, Emerging research landscape of altermagnetism. *Phys. Rev. X* **12**, 040501 (2022).

40. A. Bose, N. J. Schreiber, R. Jain, D.-F. Shao, H. P. Nair, J. Sun, X. S. Zhang, D. A. Muller, E. Y. Tsymbal, D. G. Schlom, D. C. Ralph, Tilted spin current generated by the collinear antiferromagnet ruthenium dioxide. *Nat. Electron.* **5**, 267–274 (2022).

41. H. Bai, L. Han, X. Y. Feng, Y. J. Zhou, R. X. Su, Q. Wang, L. Y. Liao, W. X. Zhu, X. Z. Chen, F. Pan, X. L. Fan, C. Song, Observation of spin splitting torque in a collinear antiferromagnetRuO2. *Phys. Rev. Lett.* **128**, 197202 (2022).

42. S. Karube, T. Tanaka, D. Sugawara, N. Kadoguchi, M. Kohda, J. Nitta, Observation of spin-splitter torque in collinear antiferromagneticRuO2. *Phys. Rev. Lett.* **129**, 137201 (2022).

43. P. J. Brown, J. B. Forsyth, V. Nunez, F. Tasset, The low-temperature antiferromagnetic structure of Mn5Si3revised in the light of neutron polarimetry. *J. Phys. Condens. Matter* **4**, 10025–10036 (1992).

44. P. Brown, J. Forsyth, Antiferromagnetism in Mn5Si3: The magnetic structure of the AF2 phase at 70 K. *J. Phys. Condens. Matter* **7**, 7619–7628 (1995).

45. M. Gottschilch, O. Gourdon, J. Persson, C. de la Cruz, V. Petricek, T. Brueckel, Study of the antiferromagnetism of Mn5Si3: An inverse magnetocaloric effect material. *J. Mater. Chem.* **22**, 15275–15284 (2012).

46. C. Surgers, G. Fischer, P. Winkel, H. V. Lohneysen, Large topological Hall effect in the non-collinear phase of an antiferromagnet. *Nat. Commun.* **5**, 3400 (2014).

47. N. Biniskos, K. Schmalzl, S. Raymond, S. Petit, P. Steffens, J. Persson, T. Bruckel, Spin fluctuations drive the inverse magnetocaloric effect in Mn5Si3. *Phys. Rev. Lett.* **120**, 257205 (2018).

48. I. Dzyaloshinsky, A thermodynamic theory of "weak" ferromagnetism of antiferromagnetics. *J. Phys. Chem. Solid* **4**, 241–255 (1958).

49. N. Nagaosa, J. Sinova, S. Onoda, A. H. MacDonald, N. P. Ong, Anomalous Hall effect. *Rev. Mod. Phys.* **82**, 1539–1592 (2010).

50. D. Xiao, M.-C. Chang, Q. Niu, Berry phase effects on electronic properties. *Rev. Mod. Phys.* **82**, 1959–2007 (2010).

51. H. Tsai, T. Higo, K. Kondou, T. Nomoto, A. Sakai, A. Kobayashi, T. Nakano, K. Yakushiji, R. Arita, S. Miwa, Y. Otani, S. Nakatsuji, Electrical manipulation of a topological antiferromagnetic state. *Nature* **580**, 608–613 (2020).

52. Y. Takeuchi, Y. Yamane, J. Y. Yoon, R. Itoh, B. Jinnai, S. Kanai, J. Ieda, S. Fukami, H. Ohno, Chiral-spin rotation of non-collinear antiferromagnet by spin-orbit torque. *Nat. Mater.* **20**, 1364–1370 (2021).

53. B. Pal, B. K. Hazra, B. Göbel, J.-C. Jeon, A. K. Pandeya, A. Chakraborty, O. Busch, A. K. Srivastava, H. Deniz, J. M. Taylor, H. Meyerheim, I. Mertig, S.-H. Yang, S. S. P. Parkin, Setting of the magnetic structure of chiral kagome antiferromagnets by a seeded spin-orbit torque. *Sci. Adv.* **8**, eabo5930 (2022).

54. A. K. Nayak, J. E. Fischer, Y. Sun, B. Yan, J. Karel, A. C. Komarek, C. Shekhar, N. Kumar, W. Schnelle, J. Kübler, C. Felser, S. S. P. Parkin, Large anomalous Hall effect driven by a nonvanishing Berry curvature in the noncolinear antiferromagnet Mn3Ge. *Sci. Adv.* **2**, e1501870 (2016).

55. J. Železný, Y. Zhang, C. Felser, B. Yan, Spin-polarized current in noncollinear antiferromagnets. *Phys. Rev. Lett.* **119**, 187204 (2017).

56. L. Liu, O. J. Lee, T. J. Gudmundsen, D. C. Ralph, R. A. Buhrman, Current-induced switching of perpendicularly magnetized magnetic layers using spin torque from the spin Hall effect. *Phys. Rev. Lett.* **109**, 096602 (2012).

57. W. Kohn, L. J. Sham, Self-consistent equations including exchange and correlation effects. *Phys. Rev.* **140**, A1133–A1138 (1965).

58. G. Kresse, J. Furthmüller, Efficient iterative schemes forab initiototal-energy calculations using a plane-wave basis set. *Phys. Rev. B* **54**, 11169–11186 (1996).

59. J. P. Perdew, K. Burke, M. Ernzerhof, Generalized gradient approximation made simple. *Phys. Rev. Lett.* **77**, 3865–3868 (1996).

60. J. P. Perdew, J. A. Chevary, S. H. Vosko, K. A. Jackson, M. R. Pederson, D. J. Singh, C. Fiolhais, Atoms, molecules, solids, and surfaces: Applications of the generalized gradient approximation for exchange and correlation. *Phys. Rev. B* **46**, 6671–6687 (1992).

61. H. J. Monkhorst, J. D. Pack, Special points for Brillouin-zone integrations. *Phys. Rev. B* **13**, 5188–5192 (1976).

62. K. Koepernik, H. Eschrig, Full-potential nonorthogonal local-orbital minimum-basis band-structure scheme. *Phys. Rev. B* **59**, 1743–1757 (1999).

63. R. F. L. Evans, W. J. Fan, P. Chureemart, T. A. Ostler, M. O. A. Ellis, R. W. Chantrell, Atomistic spin model simulations of magnetic nanomaterials. *J. Phys. Condens. Matter* **26**, 103202 (2014).

64. F. J. dos Santos, N. Biniskos, S. Raymond, K. Schmalzl, M. dos Santos Dias, P. Steffens, J. Persson, S. Blügel, S. Lounis, T. Brückel, Spin waves in the collinear antiferromagnetic phase ofMn5Si3. *Phys. Rev. B* **103**, 024407 (2021).

65. N. Biniskos, F. J. dos Santos, K. Schmalzl, S. Raymond, M. dos Santos Dias, J. Persson, N. Marzari, S. Blügel, S. Lounis, T. Brückel, Complex magnetic structure and spin waves of the noncollinear antiferromagnet Mn5Si3. *Phys. Rev. B* **105**, 104404 (2022).

66. R. F. L. Evans, U. Atxitia, R. W. Chantrell, Quantitative simulation of temperature-dependent magnetization dynamics and equilibrium properties of elemental ferromagnets. *Phys. Rev. B* **91**, 144425 (2015).

67. H. Sato, M. Yamanouchi, K. Miura, S. Ikeda, H. D. Gan, K. Mizunuma, R. Koizumi, F. Matsukura, H. Ohno, Junction size effect on switching current and thermal stability in CoFeB/MgO perpendicular magnetic tunnel junctions. *Appl. Phys. Lett.* **99**, 042501 (2011).

68. H. Sato, E. C. I. Enobio, M. Yamanouchi, S. Ikeda, S. Fukami, S. Kanai, F. Matsukura, H. Ohno, Properties of magnetic tunnel junctions with a MgO/CoFeB/Ta/CoFeB/MgO recording structure down to junction diameter of 11 nm. *Appl. Phys. Lett.* **105**, 062403 (2014).

69. W. Wernsdorfer, B. Doudin, D. Mailly, K. Hasselbach, A. Benoit, J. Meier, J. P. Ansermet, B. Barbara, Nucleation of magnetization reversal in individual nanosized nickel wires. *Phys. Rev. Lett.* **77**, 1873–1876 (1996).

70. F. Cayssol, D. Ravelosona, C. Chappert, J. Ferré, J. P. Jamet, Domain wall creep in magnetic wires. *Phys. Rev. Lett.* **92**, 107202 (2004).

71. H. Bai, W. Zhu, Y. You, X. Chen, X. Zhou, F. Pan, C. Song, Size-dependent anomalous Hall effect in noncollinear antiferromagnetic Mn3Sn films. *Appl. Phys. Lett.* **117**, 052404 (2020).

72. Y. Sato, Y. Takeuchi, Y. Yamane, J.-Y. Yoon, S. Kanai, J. I. Ieda, H. Ohno, S. Fukami, Thermal stability of non-collinear antiferromagnetic Mn_3Sn nanodot. *Appl. Phys. Lett.* **122**, 122404 (2023).

73. S. Dong, H. Xiang, E. Dagotto, Magnetoelectricity in multiferroics: A theoretical perspective. *Natl. Sci. Rev.* **6**, 629–641 (2019).

74. X. He, N. Helbig, M. J. Verstraete, E. Bousquet, TB2J: A python package for computing magnetic interaction parameters. *Comput. Phys. Commun.* **264**, 107938 (2021).

75. A. I. Liechtenstein, M. I. Katsnelson, V. P. Antropov, V. A. Gubanov, Local spin density functional approach to the theory of exchange interactions in ferromagnetic metals and alloys. *J. Magn. Magn. Mater.* **67**, 65–74 (1987).